

The growth of super-Earths: the importance of a self-consistent treatment of disc structures and pebble accretion

Sofia Savvidou and Bertram Bitsch

Max-Planck-Institut für Astronomie, Königstuhl 17, 69117 Heidelberg, Germany

Received date / Accepted date

ABSTRACT

The conditions in the protoplanetary disc are determinant for the various planet formation mechanisms. We present a framework which combines self-consistent disc structures with the calculations of the growth rates of planetary embryos via pebble accretion, in order to study the formation of Super-Earths. We first perform 2D hydrodynamical simulations of the inner discs, considering a grain size distribution with multiple chemical species and their corresponding size and composition dependent opacities. The resulting aspect ratios are almost constant with orbital distance, resulting in radially constant pebble isolation masses, the mass where pebble accretion stops. This supports the "peas-in-a-pod" constraint from the Kepler observations. The derived pebble sizes are used to calculate the growth rates of planetary embryos via pebble accretion. Discs with low levels of turbulence (expressed through the α -viscosity) and/or high dust fragmentation velocities allow larger particles, hence lead to smaller pebble isolation masses, and the contrary. At the same time, small pebble sizes lead to low accretion rates. We find that there is a trade-off between the pebble isolation mass and the growth timescale with the best set of parameters being an α -viscosity of 10^{-3} and a dust fragmentation velocity of 10 m/s, mainly for an initial gas surface density (at 1 AU) greater than 1000 g/cm^2 . A self-consistent treatment between the disc structures and the pebble sizes is thus of crucial importance for planet formation simulations.

Key words. protoplanetary discs – planets and satellites: formation – circumstellar matter – hydrodynamics – turbulence

Use \titlerunning to supply a shorter title and/or \authorrunning to supply a shorter list of authors.

1. Introduction

Observational data have so far shown that planets of a few Earth masses are one of the most abundant groups of planets in the exoplanetary systems (e.g. Borucki et al. 2010; Batalha et al. 2013; Fressin et al. 2013; Petigura et al. 2013; Mulders et al. 2018). Additionally, the super-Earth planets have been recently shown to be of similar sizes within the same planetary system (Weiss et al. 2018), even though this was put into question by an other analysis (Zhu et al. 2018). It is, therefore, of utmost interest to understand the mechanisms leading to their formation, especially given the fact that Super Earths are absent from the Solar System (Martin & Livio 2015).

The formation of planets is initiated by the coagulation (Weidenschilling 1980, 1984; Brauer et al. 2008; Zsom et al. 2011; Birnstiel et al. 2012; Testi et al. 2014), condensation (Ros & Johansen 2013) of small dust particles or nucleation on icy particles (Ros et al. 2019). There are several conditions which limit the dust growth, such as the fragmentation barrier, the bouncing barrier and the radial drift barrier (Brauer et al. 2007; Birnstiel et al. 2010; Zsom et al. 2010). However, these barriers help in the rapid formation of millimeter- to centimeter-sized particles or pebbles, which is an essential contributor to planet formation.

Planet formation can continue with the creation of larger bodies, e.g. by the streaming instability, where the dust particles concentrate into filaments with sufficient densities to gravitationally collapse into planetesimals (Youdin & Goodman 2005; Johansen & Youdin 2007; Youdin & Johansen 2007; Chiang &

Youdin 2010). In the classical core accretion scenario, the sufficiently large planetesimals serve as planetary embryos which accrete other planetesimals in order to form the planetary cores (Pollack et al. 1996; Helled et al. 2014, for a review). However, this procedure has some drawbacks, among others the growth timescale, which can be even longer than the lifetime of the protoplanetary disc (Pollack et al. 1996; Rafikov 2004; Levison et al. 2010; Lambrechts & Johansen 2012; Fortier et al. 2013; Johansen & Bitsch 2019), unless the dust density is significantly enhanced (Kobayashi et al. 2011).

One of the proposed mechanisms to form super-Earths is the accretion of pebbles, the millimeter to centimeter sized particles, onto a preexisting planetesimal or protoplanet (Johansen & Lacerda 2010; Ormel & Klahr 2010; Lambrechts & Johansen 2012; Ormel et al. 2017; Johansen & Lambrechts 2017). The accretion of solids is not limited by the available material closely around the planetary seed, but it is aided by the drift of small solids, or pebbles (Weidenschilling 1977). Pebble accretion thus acts on much shorter timescales compared to planetesimal accretion, especially in the outer disc regions (Lambrechts & Johansen 2014; Bitsch et al. 2015; Lambrechts et al. 2019; Izidoro et al. 2019; Johansen & Bitsch 2019).

In this work, we will focus on the accretion of the small particles by an already formed planetary seed. The planet grows until it reaches the pebble isolation mass (Morbidelli & Nesvorniy 2012; Lambrechts et al. 2014; Ataiee et al. 2018; Bitsch et al. 2018; Surville et al. 2020), at which it carves a gap in the protoplanetary disc, thus trapping the pebbles in a pressure trap exterior to the planet. This critical mass depends on the disc parameters, mainly the aspect ratio and not on the available amount of

Send offprint requests to: S. Savvidou,
e-mail: savvidou@mpia.de

solids. Wu (2019) showed that protoplanetary cores could grow to the thermal mass in discs, which corresponds to the typical masses of planets in the mass-constrained sub-sample of the Kepler systems. Bitsch (2019) expanded on this, showing that the pebble isolation mass could be the main driver for this observation, with a crucial dependence on the underlying protoplanetary disc structure.

The protoplanetary disc structure, thus, holds most of the key parameters and conditions which define the planet formation mechanisms. On the other hand, the grain size distribution and the subsequent opacity plays a very important role in the determination of the disc structure and the disc evolution (Savvidou et al. 2020). A change in opacity directly affects the cooling rate of the disc and the new thermal structure leads to an updated grain size distribution. The opacity of the disc is then altered because the mass fractions of the grain sizes are different. This feedback loop operates until the disc reaches thermal equilibrium, which means that the resulting disc structure is heavily influenced by the grain size distribution and the opacity provided by the dust grains (Savvidou et al. 2020) and will then determine the evolution of planet formation.

In this work, we obtain disc models from hydrodynamical simulations, including self-consistent grain distribution and opacities according to the grain sizes and compositions, following our previous work (Savvidou et al. 2020). We thus have a framework present that allows a self consistent disc structure with the corresponding pebble sizes to calculate the growth rates of planetary embryos via pebble accretion. We focus on the innermost parts of a disc to study how the grain size distribution and the chemical compositions of the grains affect the formation of super-Earths.

This paper is structured as follows. In Sect. 2 we discuss the different aspects of our model. Specifically, the opacity prescription and the chosen chemical compositions, the grain size distribution model, the disc parameters and the prescription for planet growth. In Sect. 3 we present the resulting disc structures from the self-consistent hydrodynamical simulations. We then discuss the pebble isolation masses of planets which could grow in the discs of our model and their growth timescales in Sect. 4. We discuss the implications and limitations of our model in Sect. 5 and summarize our findings in Sect. 6.

2. Methods

2.1. Opacities

We calculate the mean Rosseland, Planck, and stellar opacities as a function of temperature using the RADMC-3D¹ code. These mean opacities are used in the energy equations of the protoplanetary disc model. In particular, the energy time evolution utilizes the Planck mean opacity which uses as a weighting function the Planck black body radiation energy density distribution ($B_\lambda(\lambda, T)$). The radiation flux is inversely proportional to the Rosseland mean opacity, which is calculated using the temperature derivative of the Planck distribution ($\partial B_\lambda(\lambda, T)/\partial T$). Therefore, in contrast to the Planck mean opacity, the Rosseland mean opacity describes well the optically thick regions.

For both of the aforementioned opacities the temperature taken into account is the local disc temperature. However, when we want to describe the absorption of stellar photons, we use the stellar mean opacities, which are calculated in a similar manner

¹ <http://www.ita.uni-heidelberg.de/~dullemond/software/radmc-3d/>

to the Planck mean opacities, taking into account the temperature of the stellar radiation ($B_\lambda(T_\star)$), assuming isotropic radiation, which in our models is $T_\star = 4370$ K.

In contrast to our previous work (Savvidou et al. 2020), where only water-ice and silicates were used, we have included here all of the major rock- and ice- forming species. We present them, along with their volume mixing ratios and mass fractions in Table 1, following Bitsch & Battistini (2020). We discuss in detail how we obtained these opacities in Appendix A. In Fig. 1 we show the opacity as a function of temperature for six representative grain sizes. The gray, vertical, dashed lines correspond to the evaporation fronts for the species we include in our model. After each evaporation front, the corresponding species sublimates and no longer contributes to the overall opacity, so the mass fractions are adjusted accordingly.

2.2. Hydrodynamical simulations

The viscosity in the simulations follows an α prescription (Shakura & Sunyaev 1973). We run simulations with three α -viscosity values, namely $\alpha = 10^{-3}$, 5×10^{-4} and 10^{-4} and list all parameters of the model in Table 2.

The gas surface density follows a profile

$$\Sigma_g = \Sigma_{g,0} \cdot (r/AU)^{-p}, \quad (1)$$

with $p = 1/2$. For each α -viscosity we run a set of four initial gas surface densities, $\Sigma_{g,0} = 100, 500, 1000$ and 2000 g/cm².

In all of the simulations, the stellar mass is $M_\star = 1 M_\odot$, the stellar temperature is $T_\star = 4370$ K, and the stellar radius is $R_\star = 1.5 R_\odot$. The total dust-to-gas ratio is $f_{DG} = 1.5\%$. The discs extend from 0.1 to 4 AU, except for the simulations with $\Sigma_{g,0} = 2000$ g/cm², where the inner boundary is at 0.2 or 0.3 AU. We do not include gas opacities in our model, hence this was a necessary choice to prevent the overheating of the innermost edge and a strong shadowing that would cool down the rest of the disc. The simulations run until they reach thermal equilibrium. The disc structures from the hydrodynamical simulations are used afterwards to determine the pebble isolation masses and the pebble accretion rates, which we discuss in the following sections.

2.3. Grain size distribution

In this work we use the MRN distribution² (Mathis et al. 1977), where the normalized vertically integrated dust surface densities are calculated at each orbital distance as

$$\tilde{\Sigma}_{d,s_i} = \frac{s_i^{1/2} f_{DG,r} \Sigma_g}{\sum_i s_i^{1/2}}, \quad (2)$$

with s_i the grain size and Σ_g the gas density. In order to calculate these dust surface densities, we consider the evaporation of the chemical species as we move further-in in the disc and use $f_{DG,r}$, which is the appropriate fraction of the total dust-to-gas ratio of the disc depending on how many species have evaporated at the given location (Fig. 2).

It is important to note that we do not use a constant upper boundary for the grain sizes. Instead, we use the local disc parameters to calculate the fragmentation barrier as follows

$$s_{max} = \frac{2\Sigma_g}{3\pi\alpha_s} \frac{u_f^2}{c_s^2}, \quad (3)$$

² We found that the disc structure in itself is only slightly influenced if a more complex grain size distribution (Birnstiel et al. 2011) is used (Savvidou et al. 2020). For simplicity we use the MRN distribution.

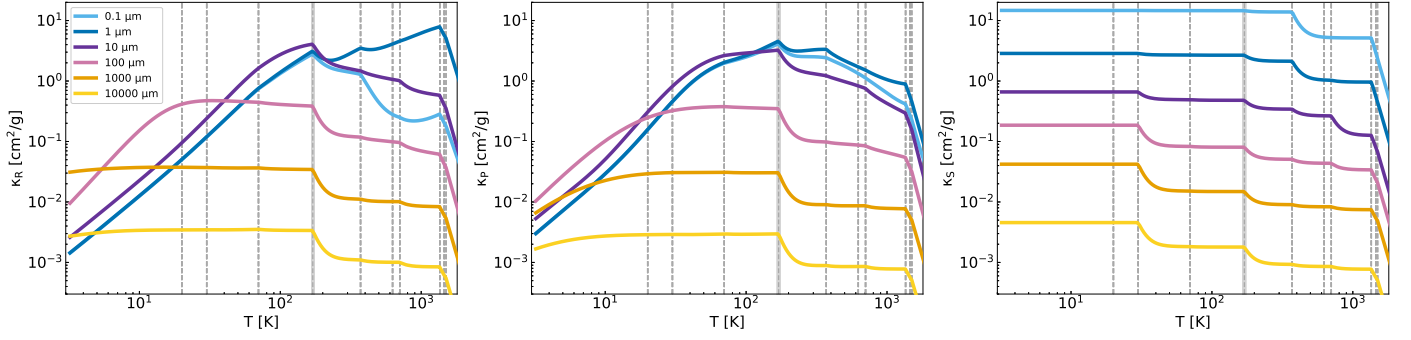


Fig. 1: Rosseland, Planck, and stellar mean opacities (from left to right) as a function of temperature for grains of sizes 0.1, 1, 10, 100 μm , 1 mm, and 1 cm. The composition of the grain mixture is presented in Table 1. The gray dashed lines show the evaporation temperature of the different species, which are from the lowest to the highest temperature: CO , CH_4 , CO_2 , H_2O , Fe_3O_4 , C , FeS , Mg_2SiO_4 , Fe_2O_3 , MgSiO_3 . We emphasize the water-ice evaporation front with an additional gray band.

Table 1: Condensation temperatures and volume mixing ratios for the chemical species used in this work. We also show the densities and mass fractions considered to calculate the mean opacities as a function of temperature, along with the references of the refractive indices.

Species	T_{cond} [K]	ρ_s [g/cm ³]	Volume mixing ratios	Mass fraction	Reference for refractive indices
CO	20	1.0288	$0.45 \times \text{C}/\text{H}$	21.68%	1, \diamond
CH ₄	30	0.47	$0.25 \times \text{C}/\text{H}$	6.882%	1, \diamond
CO ₂	70	1.5	$0.1 \times \text{C}/\text{H}$	7.574%	1, \diamond
H ₂ O	170	1.0	$\text{O}/\text{H} - (3 \times \text{MgSiO}_3/\text{H} + 4 \times \text{Mg}_2\text{SiO}_4/\text{H} + \text{CO}/\text{H} + 2 \times \text{CO}_2/\text{H} + 3 \times \text{Fe}_2\text{O}_3/\text{H} + 4 \times \text{Fe}_3\text{O}_4/\text{H})$	21.28%	2, \bullet
Fe ₃ O ₄	371	5.0	$(1/6) \times (\text{Fe}/\text{H} - \text{S}/\text{H})$	4.231%	3, \star
C	626	2.1	$0.2 \times \text{C}/\text{H}$	4.129%	4
FeS	704	4.84	S/H	6.908%	5, \star
Mg ₂ SiO ₄	1354	3.275	$\text{Mg}/\text{H} - \text{Si}/\text{H}$	13.45%	6, \star
Fe ₂ O ₃	1357	5.24	$0.25 \times (\text{Fe}/\text{H} - \text{S}/\text{H})$	4.377%	3, \star
MgSiO ₃	1500	3.2	$\text{Mg}/\text{H} - 2 \times (\text{Mg}/\text{H} - \text{Si}/\text{H})$	9.489%	6, \star

References: [1] [Hudgins et al. \(1993\)](#), [2] [Warren & Brandt \(2008\)](#), [3] Amaury H.M.J. Triaud; unpublished, [4] [Preibisch et al. \(1993\)](#), [5] [Henning & Mutschke \(1997\)](#), [6] [Jäger et al. \(2003\)](#)

Data can be found in: [\diamond] <http://vizier.u-strasbg.fr>, [\bullet] https://atmos.uw.edu/ice_optical_constants/, [\star] <https://www.astro.uni-jena.de/Laboratory/OCDB/>

with $\rho_s = 1.6 \text{ g/cm}^3$ the assumed density of each particle, u_f the fragmentation threshold velocity and c_s the sound speed.

The threshold velocity u_f corresponds to the threshold after which collisions between particles always lead to fragmentation ([Poppe et al. 2000](#)). In this work, we test two different fragmentation velocities, $u_f = 1 \text{ m/s}$ and $u_f = 10 \text{ m/s}$, corresponding to the limits of laboratory experiments ([Gundlach & Blum 2015](#); [Musiolik & Wurm 2019](#)).

2.4. Pebble accretion

We start the planetary seeds at $0.01 M_\oplus$, assuming they have already formed before. For simplicity we only take the Hill regime into account, which should start around this planetary mass ([Johansen & Lambrechts 2017](#)) and we follow the [Lambrechts & Johansen \(2014\)](#) accretion recipes. This implies that the accretion radius and the accretion rates of the planet are determined by the Stokes numbers of the pebbles

$$St_{\text{mid}} = \frac{\pi \rho_s s}{2 \Sigma_g}. \quad (4)$$

α	$\Sigma_{g,0}$ [g/cm ²]	u_f [m/s]
10^{-3}	100	1
5×10^{-4}	500	
10^{-4}	1000	10
	2000	
M_\star	1 M_\odot	
T_\star	4370 K	
R_\star	1.5 M_\odot	
total f_{DG}	1.5%	

Table 2: Parameters used in the simulations

We use for the planet growth only the Stokes numbers at mid-plane for consistency because this is the approximation we follow in our hydrodynamical models (see a more detailed discussion on the vertical distribution of the grains in Savvidou et al. (2020)). The range of grain sizes at each location of the disc is determined by the local disc properties (see maximum grain size, Eq. 3).

To define the pebble accretion rate we need to distinguish between the 2D and the 3D regime, depending on how the pebble scale height H_d compares to the effective accretion radius of the planet $(St/0.1)^{1/3} r_{Hill}$, where the Hill radius is

$$r_{Hill} = r \left(\frac{M_p}{3M_\odot} \right)^{1/3}. \quad (5)$$

The 2D pebble accretion rate is

$$\dot{M}_{2D} = 2 \left(\frac{St_{mid}}{0.1} \right)^{2/3} r_{Hill} v_{Hill} \Sigma_d, \quad (6)$$

with $v_{Hill} = \Omega r_{Hill}$, $\Omega = \sqrt{GM_\odot/r^3}$ and the 3D accretion rate is

$$\dot{M}_{3D} = \dot{M}_{2D} \left[\frac{\pi \left(\frac{St_{mid}}{0.1} \right)^{1/3} r_{Hill}}{2 \sqrt{2\pi} H_d} \right]. \quad (7)$$

The transition from the 2D to the 3D regime happens when

$$\frac{\pi \left(\frac{St_{mid}}{0.1} \right)^{1/3} r_{Hill}}{2 \sqrt{2\pi} H_d} < 1, \quad (8)$$

following Morbidelli et al. (2015). The dust scale height is derived by Dubrulle et al. (1995)

$$H_d = H_g \sqrt{\frac{\alpha}{\alpha + St}}. \quad (9)$$

We calculate the accretion rates in the 2D and 3D regime for each grain size of the distribution (Eq. 2) and then add up all of the contribution to get the total accretion rate.

Within this approach, we assume that the pebbles that are accreted by the planet are replenished at the planet's location by radial drift, so that the dust surface density does not change at the planets location during pebble accretion. Future work has to consider the grain drift and its influence on the disc's structure with accreting planets more accurately.

2.5. Pebble isolation mass

Planetary growth halts when the planet reaches the pebble isolation mass. At this mass, the planet has accreted enough material so that it carves a gap in the gas of the protoplanetary disc and creates a pressure bump around it (Paardekooper & Mellema 2006). This bump prevents the dust from drifting onto the planet core and growth via pebble accretion stops (Morbidelli & Nesvorný 2012; Lambrechts et al. 2014; Bitsch et al. 2018; Ataiee et al. 2018; Surville et al. 2020).

The pebble isolation mass has been approximated via hydrodynamical simulations by Bitsch et al. (2018) as

$$M_{iso} = 25 f_{fit} M_\oplus, \quad (10)$$

with

$$f_{fit} = \left[\frac{H/r}{0.05} \right]^3 \left[0.34 \left(\frac{\log(0.001)}{\log(\alpha)} \right)^4 + 0.66 \right] \left[1 - \frac{\frac{\partial \ln P}{\partial \ln r} + 2.5}{6} \right], \quad (11)$$

where $\frac{\partial \ln P}{\partial \ln r}$ is the radial pressure gradient. Here, we let the planets grow via pebble accretion until they reach the pebble isolation mass and track the time it takes them, to monitor if the planet can reach this mass during the disc's lifetime. However, we stop the growth at 100 Myr as this time exceeds the lifetime of protoplanetary discs quite clearly (e.g. Mamajek 2009).

2.6. Advantages and limitations of our model

Compared to 1D models, our 2D model has the advantage that the vertical structure is solved self-consistently. Furthermore, shadowing effects inside the disc caused by bumps in the disc structure that block stellar irradiation are self-consistently resolved, leading to an accurate thermal disc structure, which is not possible in 1D models. The 2D models (radial-azimuthal) of Drażkowska et al. (2019) take into account the full coagulation and drift of particles, but are limited to the isothermal approach, thus ignoring the feedback of the grain size distribution on the thermal disc structure.

1D models, on the other hand, have the possibility to be evolved over several Myr, which is not possible with our 2D models. These 1D models (Birnstiel et al. 2012) can then accurately resolve the time evolution of the grain size distribution and additionally investigate pile-ups of material in the inner disc in time, but they can not accurately model shadowing effects. Furthermore, 1D models that self consistently takes into account grain growth, grain drift, the corresponding grain opacities and the resulting thermal structure of the disc do not exist, yet. We thus show simulations with increased dust-to-gas ratios in Sect. 4 corresponding to a pile-up of grains in the inner regions caused by radial drift (Brauer et al. 2008; Birnstiel et al. 2012).

Our 2D approach allows us to explore the influence of the self-consistent disc models on pebble accretion (admittedly in a simplified way) and emphasize that the grain size distributions, their corresponding sizes and composition dependent opacities, affect the disc structure and with this planet formation. This effect thus needs to be included in future planet formation simulations, which, up until now, mostly operate with disc structures independently of the pebble size distribution (e.g. Bitsch et al. 2015; Bitsch et al. 2019; Johansen & Lambrechts 2017; Venturini et al. 2020b).

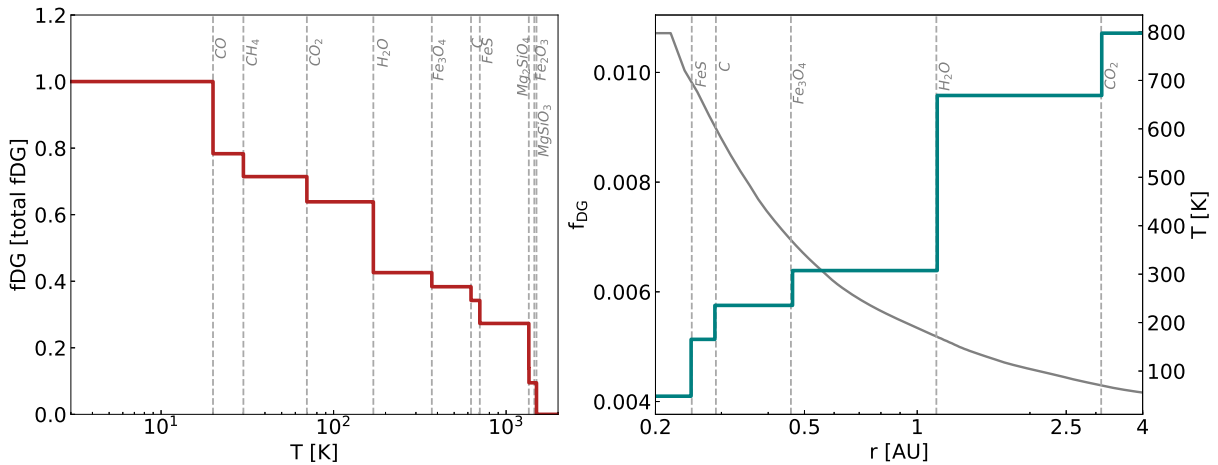


Fig. 2: Influence of the evaporation of the different chemical species on the dust-to-gas ratio in the protoplanetary disc. *Left plot:* Dust-to-gas ratio in terms of the total dust-to-gas ratio in the disc as a function of temperature. After each species evaporates the total mass fraction decreases by the corresponding mass fraction (see Table 1) until all species evaporate beyond 1500 K. *Right plot:* Example of the dust-to-gas ratio as a function of orbital distance for the disc with $\alpha = 10^{-3}$, $\Sigma_{g,0} = 2000$ g/cm² and $u_f = 10$ m/s and a global dust-to-gas ratio of 1.5%. Overplotted is the temperature of the disc where the evaporation fronts are easy to locate.

3. Disc structure

3.1. Dependence on viscosity, gas surface density and fragmentation velocity

We investigate the influence of different α -viscosities, initial gas surface density and fragmentation velocities on the grain sizes and disc structures. The specific values used are shown in Table 2. The influence of the different α -viscosity and surface densities $\Sigma_{g,0}$ to the resulting disc structure has been discussed in detail in Savvidou et al. (2020). In a nutshell, as the α -viscosity decreases, the disc gets colder for two reasons. Since the viscous heating decreases, the disc cools down more efficiently. At the same time, the dust particles face less destructive collisions and grow to larger sizes, which have lower opacities. This aids further the cooling of the disc.

We present the results of our simulations with different α parameter and for different initial gas surface densities, utilizing a fragmentation velocity of 1 m/s in Fig. 3. Clear trends with viscosity and gas surface density are visible.

Decreasing the gas surface density scales down the total dust surface density. As a consequence, the disc is colder, because the viscous heating is less efficient and radiative cooling is enhanced, given that the cooling is inversely proportional to the disc's density. However, for very low α -viscosity values the difference between discs with different surface density diminishes (Savvidou et al. 2020). We find here as well that for $\alpha = 10^{-4}$ (third column in Fig. 3), the aspect ratio of the discs is very low and almost independent of the gas surface density. In this case, the disc is mainly optically thin and the dominant heating mechanism is stellar irradiation, resulting in very similar disc structures.

The same applies to the simulations using higher fragmentation velocities. In this case, larger grains are available and dominate the opacity of the disc, hence the cooling of the disc is very efficient (Fig. 4 for $\alpha = 5 \times 10^{-4}$ and 10^{-4}). Even for the highest $\alpha = 10^{-3}$ (first column in Fig. 4), the difference in the aspect ratios of discs with varying surface densities is not as pronounced as in the corresponding discs with lower fragmentation velocity (Fig. 3). This shows that the larger grain sizes provide such low opacities that even an alpha-viscosity of 10^{-3} cannot sufficiently

heat up the disc. As a result, the water iceline is already close to 1 AU, even for the highest gas surface density.

In Figs. 3-4 we see some radial variations in some of the disc profiles, especially for very low surface densities. This is caused mainly by convection, created by the vertical temperature gradient which depends on the opacity gradient in the vertical direction and is present in the optically thick regions of the disc (Bitsch et al. 2013). However, in this work, we have included multiple chemical species in our opacity prescription, and this creates dips in the opacity as a function of temperature at the evaporation fronts of the various species³ (see Fig. 1). Even if these dips are minimal, they can create small bumps in the aspect ratio profiles which are amplified by the convection and lead to an enhancement of these perturbations.

The protoplanetary discs in our models, or regions within them, which are not strongly affected by convection, do not show a significant influence from the multiple evaporation fronts of the chemical species we have included, because the changes in the opacity are small. The strongest effect remains with the evaporation of water-ice, which causes a strong dip in the opacity and hence a more enhanced bump in the aspect ratio (Fig. 3 and 4). Nevertheless, the overall opacity is slightly different compare to a prescription where only water-ice and silicates is used (Savvidou et al. 2020). In addition to this, including multiple chemical species is important because they could be used in future work to predict the possible compositions of the planets growing within the discs of our models.

In our previous work (Savvidou et al. 2020), we discuss the dependency of the water iceline position on the α -viscosity, the gas surface density and the dust-to-gas ratio. We also find here that it moves further in if the gas surface density or the α -viscosity decreases. Here, we also use $u_f = 10$ m/s and find that the higher fragmentation velocity moves the iceline inwards compared to $u_f = 1$ m/s. This has consequences, not only for the planet formation mechanisms, but also for the potential compositions of the created planets (Bitsch et al. 2019; Schoonenberg et al. 2019; Venturini et al. 2020b). A more detailed discussion

³ In contrast, our previous simulations (Savvidou et al. 2020) only included 2 species, resulting in less variations in the disc profile.

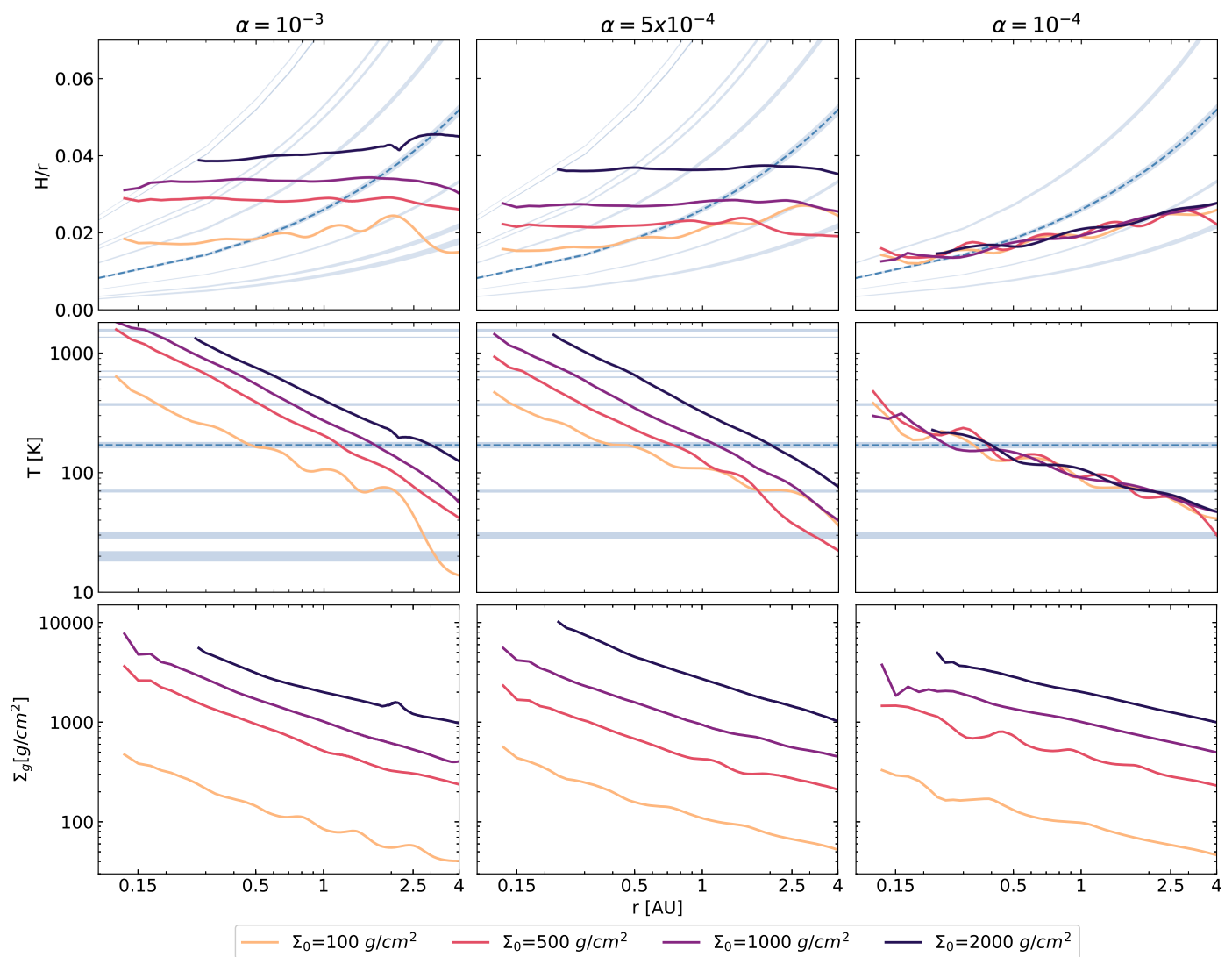


Fig. 3: Aspect ratio (upper plot), temperature (middle plot) and gas surface density (bottom plot) as a function of orbital distance for four different initial gas surface densities, from 100 g/cm^2 to 2000 g/cm^2 . The turbulence parameter in viscosity is $\alpha = 10^{-3}$ in the left panel, $\alpha = 5 \times 10^{-4}$ in the middle panel and $\alpha = 10^{-4}$ in the right panel. The fragmentation velocity is $u_f = 1 \text{ m/s}$. The light blue areas in the aspect ratio and temperature plots indicate the evaporation fronts ($\pm 2 \text{ K}$ around the evaporation temperatures of CH_4 , CO_2 and $\pm 10 \text{ K}$ for the other species). Starting from the outer boundary, for $\alpha = 10^{-3}$ the species which evaporate are CO , CH_4 , CO_2 , H_2O , Fe_3O_4 , C , FeS , Mg_2SiO_4 , MgSiO_3 . For $\alpha = 5 \times 10^{-4}$ the evaporation fronts are of CO_2 , H_2O , Fe_3O_4 , C , FeS , Mg_2SiO_4 , MgSiO_3 and for $\alpha = 10^{-4}$ they are CO_2 , H_2O , Fe_3O_4 . We highlight the water ice line with an additional dashed line.

about planet growth within the discs of our models follows in Sect. 4.

3.2. Disc evolution

Our 2D hydrodynamical models can not be integrated over several Myr due to computational limitations. Instead, the disc evolution can be mimicked by reducing the overall gas surface density, where lower disc surface densities correspond to lower stellar accretion rates and thus to older discs (Hartmann et al. 1998). As a consequence the viscous heating is reduced and the discs become colder as they age. However, assigning an absolute age to our here presented disc structures is difficult, because the exact time evolution of a disc depends on more than just the viscosity and the gas surface density, because also disc winds can drive the evolution of the disc (Bai et al. 2016; Suzuki et al. 2016).

In our model, the evaporation fronts of different solids depend on the temperature (table 1) and consequently are also closer to the central star in discs with lower gas surface density. At the evaporation fronts, solids evaporate and thus the solid surface density is reduced (Fig. 2), leading to lower opacities and thus more efficient cooling, which can cause bumps in the disc structure if the solid abundances change by a large factor, as e.g. at the water ice line. However, the maximal pebble size by fragmentation does not change, because the maximal pebble size does not depend on dust surface density (Eq. 3). As a consequence, the pebble sizes are smooth across the evaporation fronts, implying that even if disc evolution over several Myr was taken into account, it would happen smoothly and no bumps/dips will be generated at the evaporation fronts. As the disc becomes older and its surface density reduces in time, the maximal pebble size increases. We discuss the consequences of this on planet formation via pebble accretion in the next section.

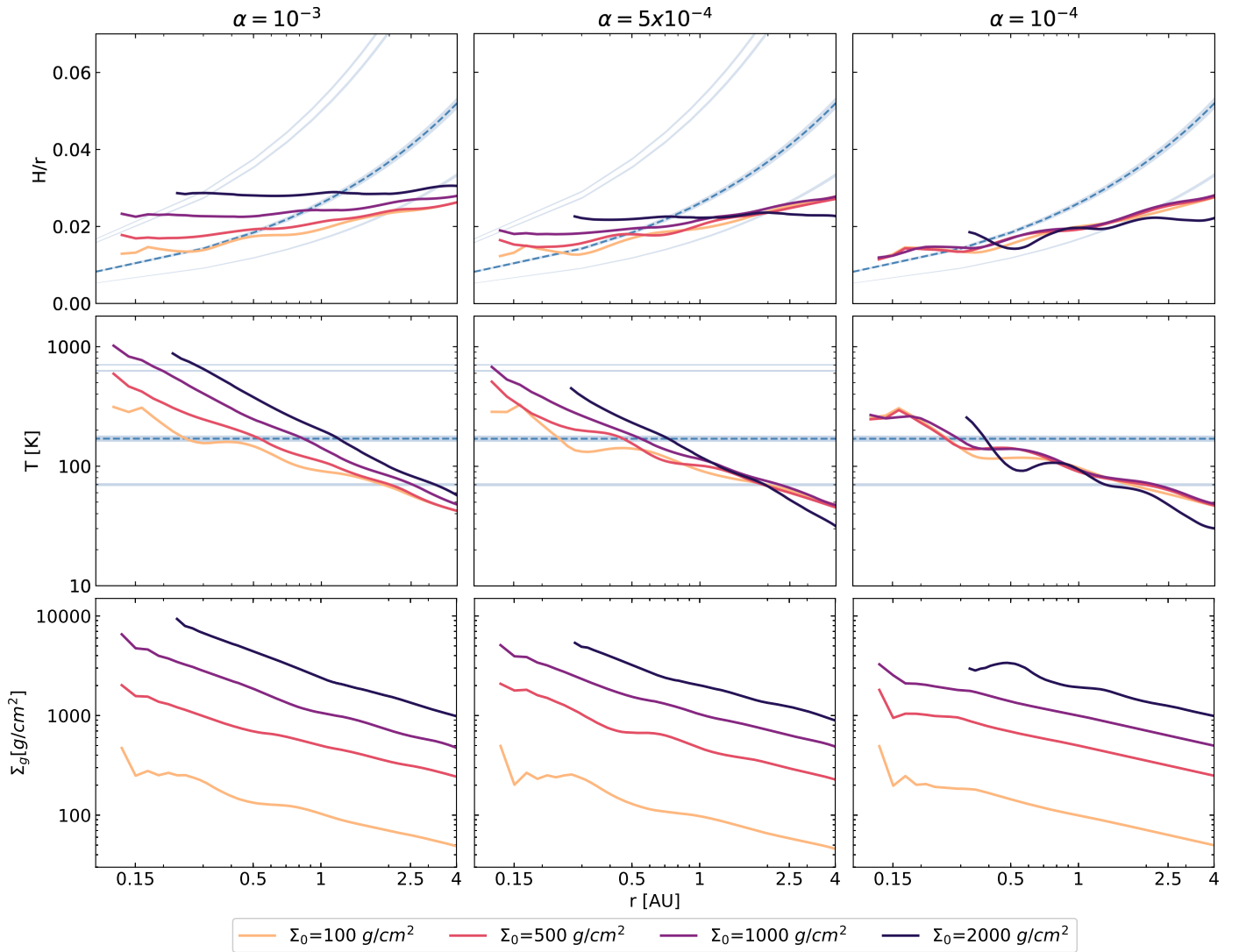


Fig. 4: Same as Fig. 3, but using a fragmentation velocity of $u_f = 10$ m/s. Starting from the outer boundary, for $\alpha = 10^{-3}$ the species which evaporate are CO_2 , H_2O , Fe_3O_4 , C , FeS . For $\alpha = 5 \times 10^{-4}$ the icelines are of CO_2 , H_2O , Fe_3O_4 , C , FeS and for $\alpha = 10^{-4}$ they are CO_2 , H_2O . The water icelines are also plotted with dashed lines.

4. Planet formation

An important implication which can be derived from the disc structures of the presented models is that the aspect ratio profiles, independently of the parameters used, are almost constant with orbital distance. This is expected in these inner regions where viscous heating dominates over stellar irradiation which would flare up the disc (Chiang & Goldreich 1997; Dullemond & Dominik 2004; Bitsch et al. 2015; Ida et al. 2016; Savvidou et al. 2020).

The implication of this observation is that the planetary systems which could potentially form in those discs would have very similar masses, since the pebble isolation mass depends on the aspect ratio (see Eq. 10). It has been recently observed among the *Kepler* systems that planets within the same system have similar sizes (Weiss et al. 2018). Millholland et al. (2017) suggested that the "peas-in-a-pod" trend is also true for the planetary masses within the same system.

We now compare the pebble isolation masses derived from our disc simulations with the super-Earth population and then discuss planetary growth within these disc environments. We

stress here again that discs with large gas surface densities could correspond to young discs, while the discs with low gas surface densities could correspond to older discs. As the exact time evolution of discs is complicated (e.g. Bai et al. 2016; Suzuki et al. 2016) and not self-consistently included in our model, we do not link our disc structures to a time evolution, but just discuss the implications of the fixed disc structures on planetary growth via pebble accretion under the simple assumption that the disc structure does not evolve in time.

4.1. Pebble isolation mass

We use the equilibrium disc structures from the 2D hydrodynamical simulations to study the growth of super-Earths via pebble accretion. It is assumed that planets will grow up to the pebble isolation mass because then they carve a gap in the protoplanetary disc and create a pressure bump exterior to their orbits which traps pebbles and prevents them from being accreted. We thus calculate the pebble isolation mass for each one of our disc models to find the maximum mass our planets could reach. The pebble isolation mass (Eq. 10) depends on the disc structure

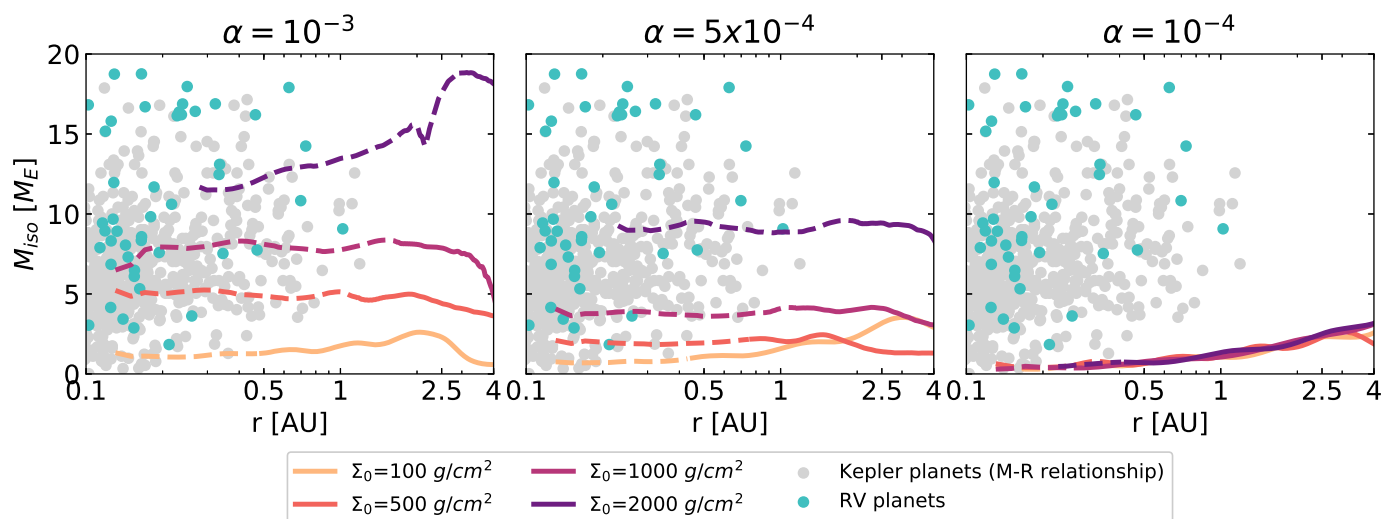


Fig. 5: Pebble isolation mass as a function of orbital distance for discs with four different initial gas surface densities, from 100 g/cm^2 to 2000 g/cm^2 . The turbulence parameter in viscosity is $\alpha = 10^{-3}$ in the left panel, $\alpha = 5 \times 10^{-4}$ in the middle panel and $\alpha = 10^{-4}$ in the right panel. The fragmentation velocity is $u_f = 1 \text{ m/s}$. We also include planetary masses of Kepler systems, with radii up to $4 R_{\oplus}$, derived through the *Forecaster* package (Chen & Kipping 2017) (grey circles) and super-Earths detected by RV (blue circles). The dashed lines correspond to the disc regions interior to the iceline, whereas the solid lines are the regions exterior to the iceline, where forming planets would be water rich.

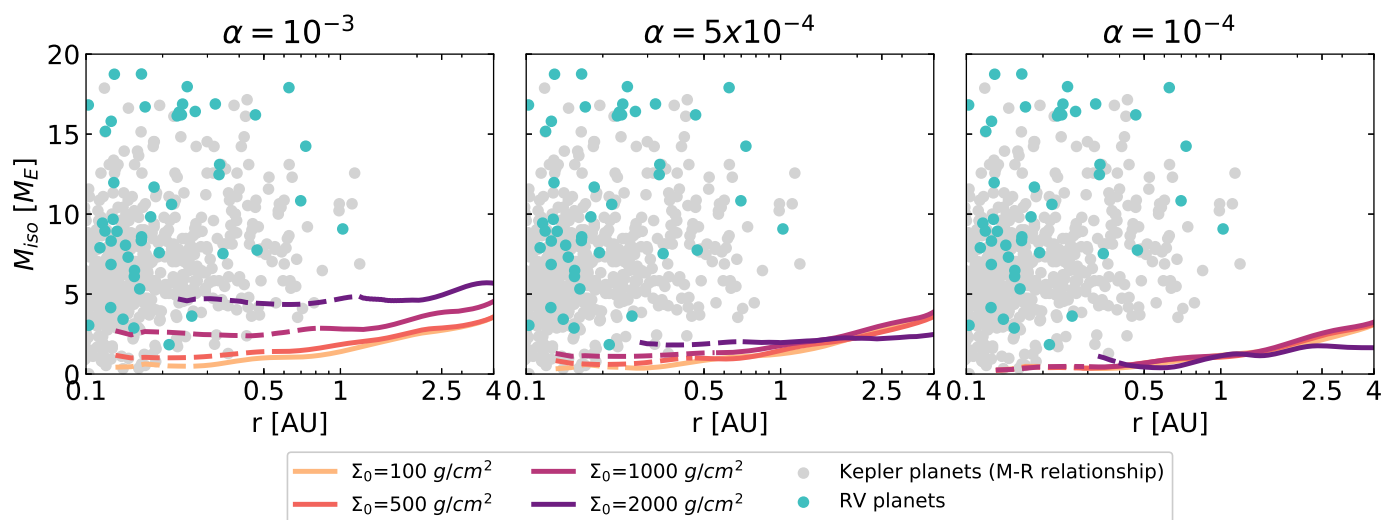


Fig. 6: Same as Fig. 5, but for a fragmentation velocity of $u_f = 10 \text{ m/s}$.

and specifically, its aspect ratio, α -viscosity and the radial pressure gradient. We present the pebble isolation mass derived from our hydrodynamical simulations in Fig. 5 and Fig. 6, where we also overplot the masses of close-in super-Earths inferred, using a mass-radius relationship (Chen & Kipping 2017), from the *Kepler* observations as well as for planets with RV mass determinations.

The aspect ratio profiles for the disc range in our models are almost constant with orbital distance, so we expect and find a low dependency of the pebble isolation mass on the orbital distance. For $\alpha = 10^{-3}$ and $u_f = 1 \text{ m/s}$ the pebble isolation mass reaches almost $19 M_{\oplus}$ for the highest initial gas surface density, $\Sigma_{g,0} = 2000 \text{ g/cm}^2$. With the same fragmentation velocity and $\alpha = 5 \times 10^{-4}$ we still get high enough isolation masses, to match the majority of the observed super-Earths / mini-Neptunes, mainly for the highest surface density,

$\Sigma_{g,0} = 2000 \text{ g/cm}^2$. However, for lower α values or higher fragmentation velocities the pebble isolation mass hardly exceeds $3\text{--}4 M_{\oplus}$. This also means that with these sets of parameters it is hard to explain the bulk of the masses of close-in super-Earths / mini-Neptunes by pure pebble accretion.

Increasing the fragmentation velocity to $u_f = 10 \text{ m/s}$, we find that the pebble isolation masses are significantly reduced. This happens because of the larger particles (Eq. 3), which lead to a smaller aspect ratio (see Sect. 3 and Eq. 10). The highest mass we find is around $5 M_{\oplus}$ for $\alpha = 10^{-3}$ and again the highest initial gas surface density, $\Sigma_{g,0} = 2000 \text{ g/cm}^2$. For the rest of the simulations, the pebble isolation mass is so low that the masses of the inner super-Earths might not be reached without a significant amount of collisions between the bodies.

Considering only the pebble isolation masses of the discs discussed here, we can conclude that in order to explain the inferred

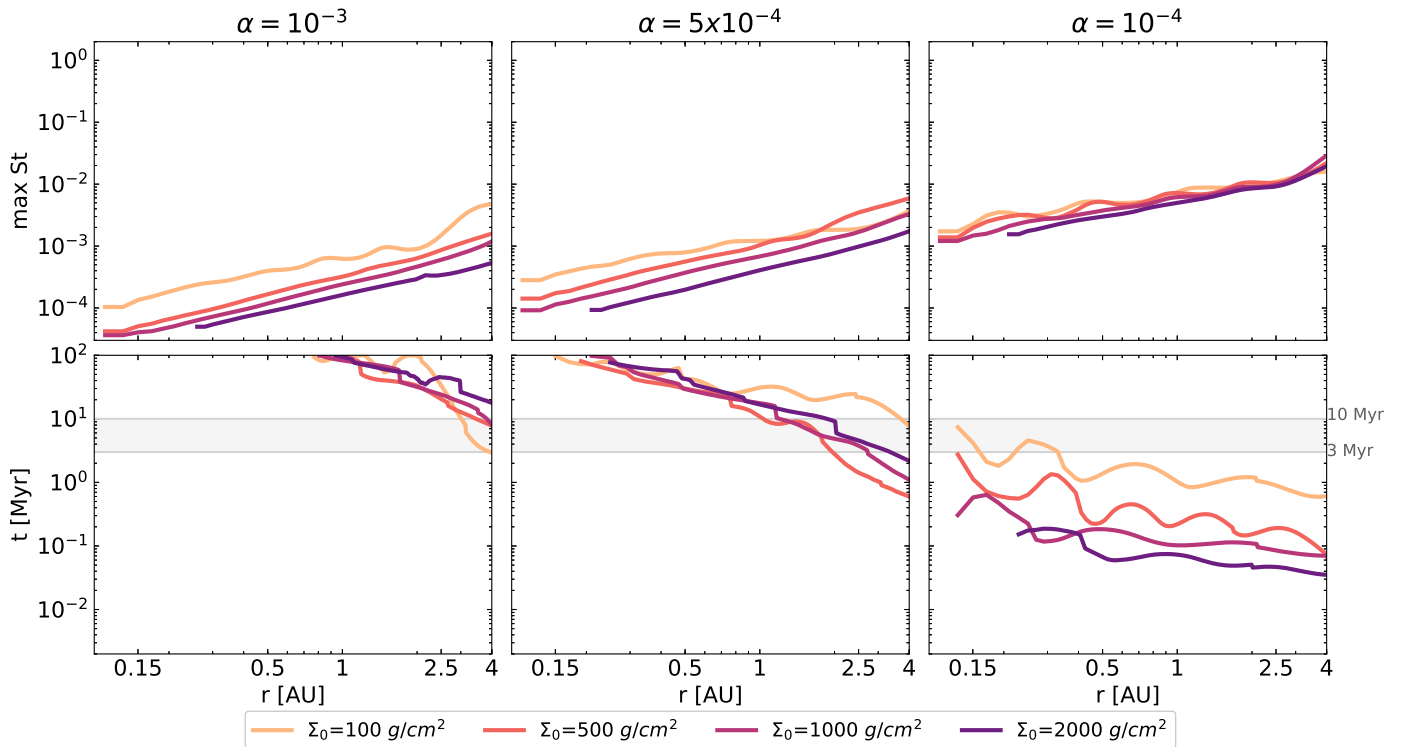


Fig. 7: Maximum Stokes number (top plot) and planetary growth timescale until the pebble isolation mass is reached (bottom plot) as a function of orbital distance, for the discs with the four different initial gas surface densities, $\alpha = 10^{-3}$ (left plot), $\alpha = 5 \times 10^{-4}$ (middle plot), $\alpha = 10^{-4}$ (right plot), and $u_f = 1$ m/s. The gray lines show the typical lifetime range of a protoplanetary disc of 3 to 10 Myr.

masses from *Kepler* detections, we would need a relatively high viscosity of $\alpha = 10^{-3}$. However, it is also important to consider whether pebble accretion can operate efficiently enough so that the planets reach these masses in a timely manner. We discuss this in the following section.

4.2. Planet growth until pebble isolation mass

To study planet growth we calculate the pebble accretion rate using Eqs. 6 and 7. The Stokes numbers are determined by the MRN distribution. For simplicity we ignore planetary migration. We show the maximum Stokes numbers as a function of orbital distance in the upper plots of Fig. 7 and 8 for all of the different parameters used. The Stokes numbers are inversely proportional to the gas density of the disc (Eq. 4). The maximum Stokes numbers are hence an increasing function of the orbital distance. They also show some radial variations for the same reason.

We show the growth timescales for our different simulations in the bottom plots of Figs. 7 and 8. These timescales represent the time it takes for the planets to reach the pebble isolation mass at the given orbital distance (Figs. 5 and 6) accreting pebbles with a size distribution corresponding to the planets location. The growth timescales are not entirely smooth. This is related, firstly, to the variations in the Stokes number (upper plots of Figs. 7 and 8 for the maximum values). Secondly, there are also some variations in the dust surface density, because of the evaporation fronts (see the steps for the dust-to-gas ratio in Fig. 2).

When considering the time it takes to reach the isolation masses it is important to compare it with the time of the gas dispersal, marked by a gray band in the bottom plots of Fig. 7 and

Fig. 8. After this event, planets can continue to grow via mutual collisions, however the formation pathway is different and if the planets have not reached sufficient masses already, they will end up being terrestrial rather than super-Earths (Lambrechts et al. 2019).

For fragmentation velocities of 1 m/s and $\alpha = 10^{-3}$, pebble accretion is inefficient in the inner disc regions (with a slight dependence on the gas surface density, Fig. 7) and thus longer than the typical lifetimes of protoplanetary discs. These timescales get significantly shorter for a decrease in the α -viscosity or an increase the fragmentation velocity to 10 m/s (Fig. 8) which allow larger grains to be accreted (Eq. 3), enhancing pebble accretion (Eqs. 6 and 7). Our simulations thus indicate that either a low α -viscosity or larger grain fragmentation velocities are needed to allow fast enough growth via pebble accretion.

In Fig. 9 we show the planetary growth of embryos located at 1 AU as a function of time, for planets growing in discs with $\Sigma_{g,0} = 2000$ g/cm² for all α -viscosities and fragmentation velocities. The planet grows fastest in environments with low viscosities and large fragmentation velocities. However, the pebble isolation mass is small in these cases. Only for cases of high α and low fragmentation velocity, is the pebble isolation mass large enough to match the observed exoplanet population.

The larger grains carry lower opacities which enhances the cooling of the disc. The low temperature also translates to a low aspect ratio (Fig. 4), hence the isolation masses are very low (Fig. 6) and even though the timescales to reach them are very short, the planets that could potentially form cannot explain the majority of the masses of super-Earths and mini-Neptunes. The best options for sufficiently large isolation masses and short growth timescales are $\alpha = 10^{-3}$, $u_f = 10$ m/s, which leads to

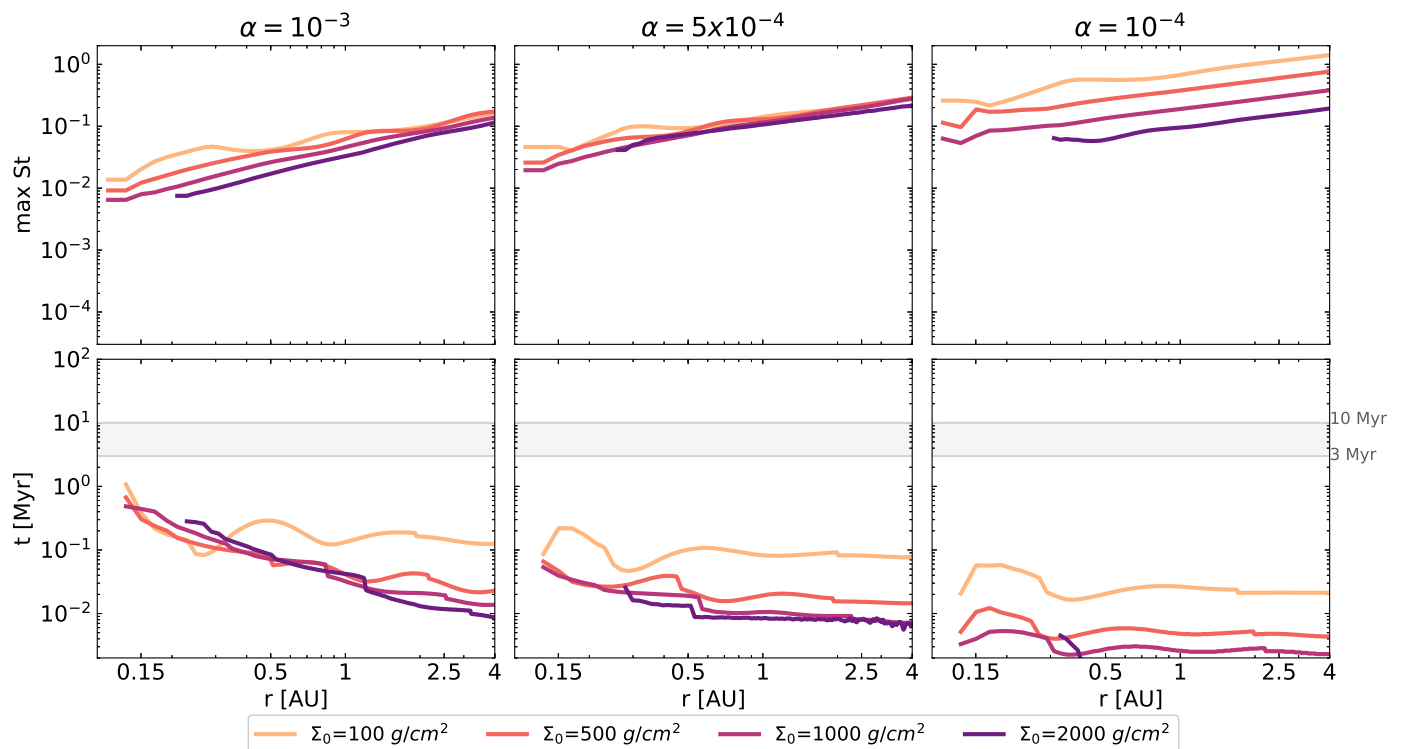


Fig. 8: Same as Fig. 7 for $u_f = 10$ m/s.

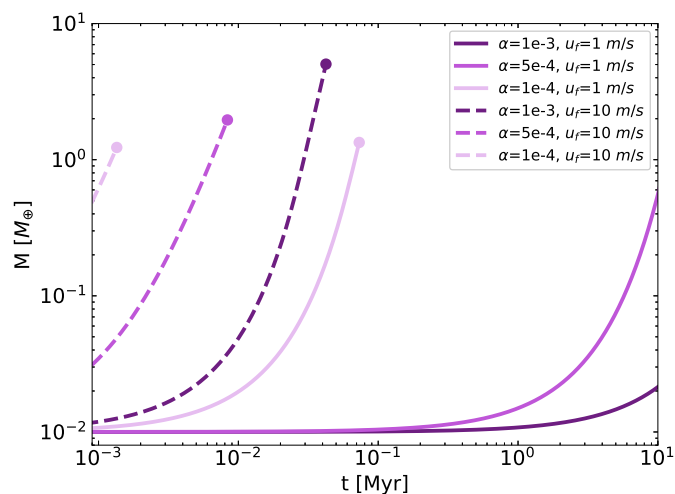


Fig. 9: Planetary mass as a function of time for the simulations with $\Sigma_{g,0} = 2000$ g/cm², all α -viscosities and both of the fragmentation velocities at 1 AU. The dot marks the final planetary mass determined by the pebble isolation mass (Figs. 5 and 6). The growth time scale is longer than 10 Myr in discs with $\alpha > 5 \times 10^{-4}$ when particle collisions are limited by a fragmentation velocity of 1 m/s.

masses from 0.4 to 5.7 M_{\oplus} , depending on the gas surface density and the orbital distance.

In the following section we will explore if planet formation at earlier stages (high gas surface densities) and higher dust-to-gas ratios could increase the pebble isolation mass, and keep the planetary growth timescales short at the same time.

4.3. Testing higher dust-to-gas ratio, gas surface density and initial planetary seed mass

We have concluded that the best parameters for Super-Earth formation via pebble accretion are $\alpha = 10^{-3}$ and $u_f = 10$ m/s. In this case, the pebble isolation mass is reached before the dispersal of the gaseous disc regardless of the surface density and the location within the disc. The isolation mass itself depends on the surface density and with the highest surface density ($\Sigma_{g,0} = 2000$ g/cm²) planets of around 5 M_{\oplus} could form by pure pebble accretion.

We investigate here how higher gas surface densities and higher dust-to-gas ratios influence the pebble isolation masses and the accretion times by pebble accretion. We show in Fig. 10 (top and middle panel) the pebble isolation masses and the maximum Stokes numbers from the additional simulations. We used two different total dust-to-gas ratios, $f_{DG} = 2\%$ and $f_{DG} = 3\%$ with $\Sigma_{g,0} = 2000$ g/cm² and a higher gas surface density, $\Sigma_{g,0} = 5000$ g/cm² with the nominal total $f_{DG} = 1.5\%$.

The difference between the nominal dust-to-gas ratio and the 2% is very small, so the pebble isolation masses are very similar. We find slightly higher pebble isolation masses with a dust-to-gas ratio of 3%, but the strongest improvement comes from the simulation with $\Sigma_{g,0} = 5000$ g/cm². In this case, the maximum pebble isolation masses can be around 11 M_{\oplus} near the outer boundary of the disc.

The growth timescales (bottom panel in Fig. 10) are also very similar between the simulation with the nominal total dust-to-gas ratio and the one with $f_{DG} = 2\%$. If we double the amount of solids ($f_{DG} = 3\%$), then the growth timescale is longer because of the larger isolation mass and the similar maximum Stokes numbers. If we increase the gas surface density to $\Sigma_{g,0} = 5000$ g/cm², there is enough material to accrete pebbles fast enough and reduce the growth timescale compared to the high dust-to-

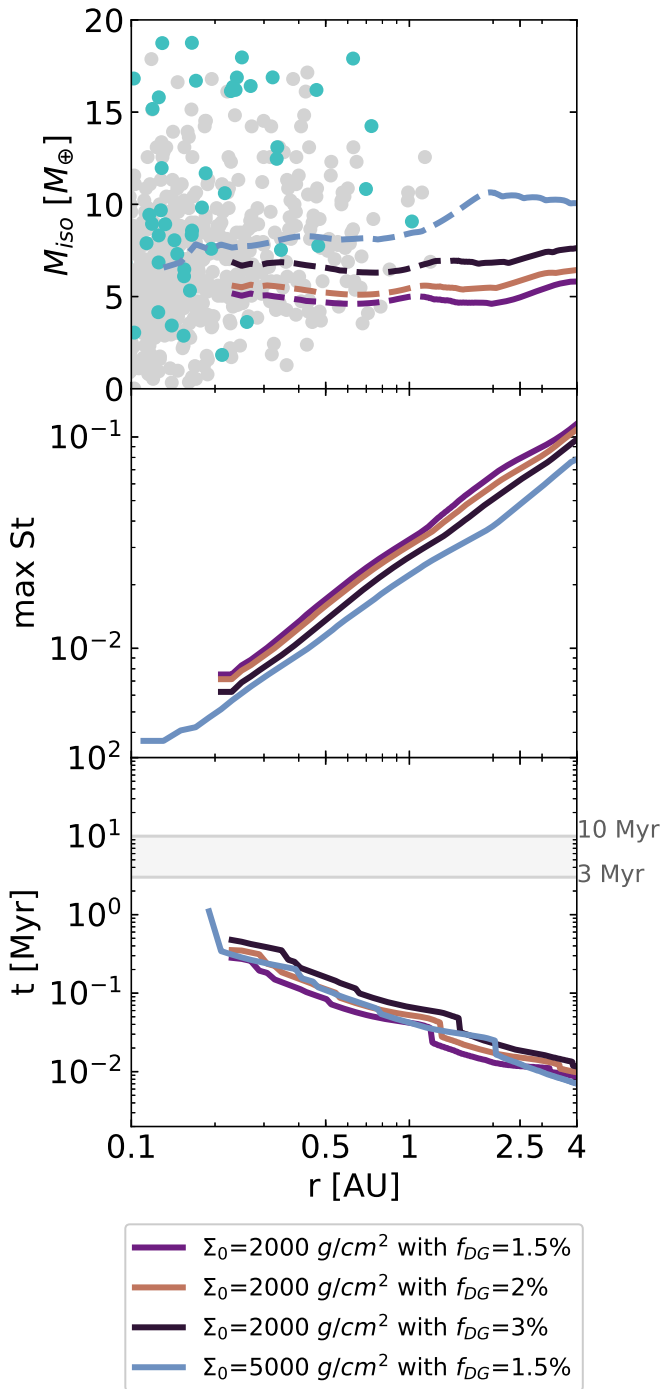


Fig. 10: Pebble isolation mass (top plot), maximum Stokes number (middle plot) and planetary growth timescale until the pebble isolation mass is reached (bottom plot) as a function of orbital distance, for discs with $\alpha = 10^{-3}$ and $u_f = 10$ m/s. We show discs with higher dust-to-gas ratios, $f_{DG} = 2\%$ and $f_{DG} = 3\%$ and higher initial surface density $\Sigma_{g,0} = 5000 \text{ g/cm}^2$. We include for reference the nominal run with $\Sigma_{g,0} = 2000 \text{ g/cm}^2$ and $f_{DG} = 1.5\%$.

gas ratio simulations, however it is very similar to the nominal simulation.

In Fig. 11 we show how the growth timescales change depending on the assumed initial mass of the planetary seed. We compare our nominal simulations with $\alpha = 10^{-3}$ and $\alpha = 5 \times$

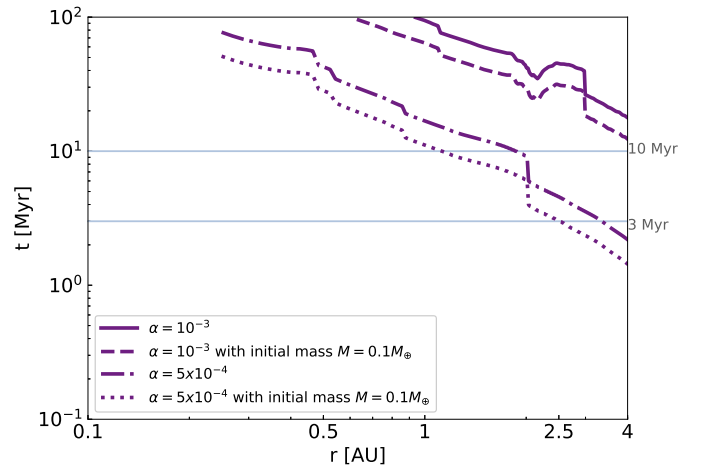


Fig. 11: Planetary growth timescale until the pebble isolation mass is reached as a function of orbital distance with initial planetary seed masses $M_{init} = 0.1 M_{\oplus}$. We tested two α -viscosities, 10^{-3} and 5×10^{-4} with a fragmentation velocity, $u_f = 1$ m/s. Overplotted are the nominal disc models with initial planetary seed masses $M_{init} = 0.01 M_{\oplus}$.

10^{-4} for $u_f = 1$ m/s and an initial planetary mass of $M_{init} = 0.01 M_{\oplus}$ with an increased initial mass of $M_{init} = 0.1 M_{\oplus}$. We only used $\Sigma_{g,0} = 2000 \text{ g/cm}^2$ because this surface density leads to the highest pebble isolation masses. The higher initial mass reduces the growth timescale, but the difference is small and for most of the regions of the inner discs the pebble isolation mass is not reached within the lifetime of the disc.

5. Discussion

5.1. Planet growth

The aspect ratios and the temperatures in our discs are relatively low, as expected by the low viscosity we have used (Savvidou et al. 2020). The same is true for the discs with higher fragmentation velocities ($u_f = 10$ m/s in contrast to $u_f = 1$ m/s) because the collisions are less destructive and the larger particles, which are allowed, carry lower opacities. In the context of pebble accretion, this means that the pebble isolation masses we calculate do not correlate sufficiently with the bulk of the planetary masses that are observations unless $\alpha = 10^{-3}$ and $u_f = 1$ m/s. In this specific case, we have small enough particles, so that the opacity is sufficient to prevent significant cooling and hence high enough aspect ratios.

However, in order to have fast growth of the planets, we need either $\alpha \leq 10^{-4}$ and $u_f = 1$ m/s or any $\alpha \leq 10^{-3}$ and $u_f = 10$ m/s (Figs. 7 and 8) since the maximum Stokes numbers are larger by up to two orders of magnitude (Figs. 5 and 6). Therefore there seems to be a trade-off between the possible pebble isolation mass and the timescale to reach it. The most efficient parameters to have both high enough isolation masses and short enough timescales are $\alpha = 10^{-3}$ and $u_f = 10$ m/s.

Venturini et al. (2020b) find that $\alpha < 10^{-4}$ is needed to reach the pebble isolation mass in time. The maximum masses they find are around $7 M_{\oplus}$ for an $\alpha = 10^{-5}$. They use slightly different parameters for their nominal runs (e.g. initial dust-to-gas ratio of 1% which can increase through radial drift in the inner disc with only small difference if the initial dust-to-gas ratio is larger) and a different disc model where dust opacities do not

contribute self-consistently to the disc model. Specifically, the dust opacities follow the [Bell & Lin \(1994\)](#) opacity law, which has been shown to produce misleading disc structures, especially when multiple grain sizes are included because they are based on micrometer sized dust ([Savvidou et al. 2020](#)). Our model suggests that a higher viscosity is needed to prevent a too low pebble isolation mass. However, their conclusions remain consistent compared to our work, regarding that a high enough Stokes number of the particles is needed to allow fast and efficient enough growth and that more massive ice rich planets can emerge from exterior to the snow line.

We do not include gas accretion into our model, because gas accretion might not be efficient for low mass planets in the inner regions of the protoplanetary disc ([Ikoma et al. 2000](#); [Lee et al. 2014](#); [Lambrechts & Lega 2017](#); [Cimerman et al. 2017](#)). Furthermore, observational constraints indicate that planets with up to 4 Earth radii have mostly only up to a few per cent of their mass in hydrogen and helium envelopes ([Zeng et al. 2019](#)). This implies that the majority of the planetary mass for these close-in super-Earths / mini-Neptunes has to originate from solid accretion, justifying as a first approach to ignore gas accretion.

5.2. Comparison to the Kepler data

We find almost flat aspect ratios independently of the disc parameters used. This is an important observation as it could lead to planetary systems with similar masses. In [Millholland et al. \(2017\)](#) it is suggested that similar masses in a system would also lead to similar radii, hence the constant with orbital distance aspect ratios we note in our discs support the "peas-in-a-pod" scheme ([Weiss et al. 2018](#)). In order to reach more specific conclusions on this matter it would be important to consider multiple growing embryos at the same time.

Judging by the almost flat, slightly flaring aspect ratios, planets allowed to migrate would be expected to migrate inwards ([Bitsch et al. 2015](#); [Savvidou et al. 2020](#)). The pebble isolation masses have a low dependency on the orbital distance, hence the maximum mass planets can reach would remain unchanged within our simulations, even if we were to include planet migration. We, nevertheless, expect discs to be flared (e.g. [Chiang & Goldreich 1997](#)), thus increasing the pebble isolation mass at larger distances to the star. The growth rate, though, is slower near the innermost regions of the discs, caused by the evaporation of solids, making growth to Super-Earth masses even harder.

It is important to include migration in future work, not only to reach more robust conclusions on the "peas-in-a-pod" configuration, but also for the role it can play in determining the composition of the planets ([Raymond et al. 2018](#); [Bitsch et al. 2019](#); [Izidoro et al. 2019](#)). Even though here we include several chemical species, we do not discuss the influence they could have on the planetary compositions.

Even if we only consider the pebble isolation masses that we find here (Fig. 5 and Fig. 6), and not whether there will be time to reach them, we notice that most of the observed planetary masses are above the pebble isolation masses in our simulations. This can be explained by our self-consistent disc model with the grain size distribution leading to aspect ratios much lower than used in previous models, due to the size and composition dependent opacities. The growth of the planets, though, can be aided by collisions, either before or after the dissipation of the gas disc ([Kominami & Ida 2004](#); [Ogihara & Ida 2009](#); [Cossou et al. 2014](#); [Izidoro et al. 2017](#); [Ogihara et al. 2018](#); [Izidoro et al. 2019](#)).

The low masses that we find could also be explained if those planets are not super-Earths, but terrestrial planets. If the peb-

ble flux is low, then we expect to have small planetary masses before the gas dissipation. Even with collisions after the gas dissipation, the masses cannot exceed a few M_{\oplus} ([Lambrechts et al. 2019](#)) which is consistent with the mass we find in this work for $\alpha = 10^{-3}$ and $u_f = 10$ m/s. However, it is important to discuss the composition of the planets to define whether they are terrestrial or super-Earths, where planets formed during the gas phase could accrete small gaseous envelopes in contrast to planets that formed similar to the terrestrial planets via collisions after the gas phase.

5.3. Disc parameters

We have explored a few pathways to either increase the pebble isolation masses or shorten the growth timescales. As a reminder, the fastest growth timescales with high enough isolation masses come from the models with $\alpha = 10^{-3}$ and $u_f = 10$ m/s. The nominal dust-to-gas ratio is 1.5%. As a consequence, we tested models with the aforementioned α -viscosity and fragmentation velocity and the highest surface density with $\Sigma_{g,0} = 2000$ g/cm² because this density provides the highest isolation masses. We also tested the nominal dust-to-gas ratio with higher surface density, $\Sigma_{g,0} = 5000$ g/cm².

We find that the higher dust-to-gas ratio, does indeed improve the isolation masses, mainly for the case with 3%, which is twice our nominal value. However, the masses remain just above 5 M_{\oplus} . The most significant improvement comes with the higher initial gas surface density. Especially near the outer boundary, the pebble isolation mass with $\Sigma_{g,0} = 5000$ g/cm² reaches approximately 10 M_{\oplus} . This implies that in order to explain the constraints of the *Kepler* observations ([Weiss et al. 2018](#)) we would need very high disc masses or a significant enhancement of the dust-to-gas ratio. Local enhancements could occur in the inner regions from radial drift (e.g. [Birnstiel et al. 2012](#)) or via pebble traps. These could be planet-induced pressure bumps or "traffic jams" at the evaporation fronts ([Ros & Johansen 2013](#); [Ida & Guillot 2016](#); [Schoonenberg & Ormel 2017](#); [Drażkowska & Alibert 2017](#); [Ros et al. 2019](#)).

In addition, it is worth noting that [Venturini et al. \(2020a\)](#) claim that the more massive inner super-Earths (the planets that would populate the second peak at larger radii in the radius distribution, e.g. [Fulton et al. \(2017\)](#)) are actually water rich planets originating from beyond the iceline, where the pebble isolation mass is larger, in agreement with our model. Migration should be included in future work in order to determine the final positions and masses of the planets.

The iceline position is located around 3 AU for $\alpha = 10^{-3}$, $\Sigma_{g,0} = 2000$ g/cm² and $u_f = 1$ m/s. Lower α -viscosities, gas surface densities or fragmentation velocities move the iceline inwards (see Sect. 3 and ([Savvidou et al. 2020](#))). The higher dust-to-gas ratios or gas surface densities, thus, also help in keeping the iceline further out from the star. However, the position and evolution of the iceline location, along with the possibility of migration for planets defines their compositions ([Bitsch et al. 2019](#)).

6. Summary

In this work, we use the self-consistent protoplanetary disc model presented in [Savvidou et al. \(2020\)](#), with additional chemical species and the corresponding opacities (see Table 1 and Fig. 1), focusing on the inner parts of the disc. We use the MRN grain size distribution ([Mathis et al. 1977](#)), with a disc-dependent upper boundary for the grain sizes (Eq. 3). We then combine the

equilibrium disc structures from the hydrodynamical simulations with a framework to study planet growth via pebble accretion. The disc parameters we used are summarized in Table 2. In this work, we do not take into account planetary migration and do not discuss the planetary compositions for simplicity. Furthermore, because the growing planets are in the low mass regime we do not model gas accretion. Additionally we use only fixed disc structures in time, because our 2D model can not be evolved for several Myr.

We present the equilibrium disc structures in Figs. 3 and 4. The aspect ratio profiles are almost constant with orbital distance. This is expected because at these innermost parts of the protoplanetary discs, viscous heating dominates over stellar irradiation and the disc does not flare up (Chiang & Goldreich 1997; Dullemond & Dominik 2004; Bitsch et al. 2015; Ida et al. 2016; Savvidou et al. 2020). This implies that the planets forming in the inner disc would have similar masses in the pebble accretion scenario, because the pebble isolation mass is a strong function of the aspect ratio, supporting the "peas-in-a-pod" scheme (Millholland et al. 2017; Weiss et al. 2018).

We calculate the pebble isolation masses following the approximation by Bitsch et al. (2018) (Figs. 5 and 6) and then estimate the time it takes to reach them depending on the disc parameters (Figs. 7 and 8). Including opacities which are grain size and composition dependent means that when the disc parameters allow large particles to form, the aspect ratios will be lower. This leads to low pebble isolation masses because they directly depend on the aspect ratio of the disc (Eq. 10). We find the highest pebble isolation masses for $\alpha = 10^{-3}$ and 5×10^{-4} when the fragmentation velocity is $u_f = 1$ m/s and for $\alpha = 10^{-3}$ when $u_f = 10$ m/s, mainly for high gas surface densities, with $\Sigma_{g,0} \geq 1000$ g/cm².

However, high pebble isolation masses also mean longer growth timescales, because of the smaller pebbles inside the disc. Comparing with the typical lifetimes of protoplanetary discs (3 to 10 Myr), we find that for low fragmentation velocities ($u_f = 1$ m/s) the timescales for planetary growth are too long (with a small dependence on the gas surface density and the orbital distance). Hence, there is a trade-off between the pebble isolation masses and the growth timescales and we conclude that the best set of parameters is $\alpha = 10^{-3}$ and $u_f = 10$ m/s within our model. With a gas surface density of $\Sigma_{g,0} = 2000$ g/cm² the pebble isolation masses reach almost $6 M_{\oplus}$, which the planets can reach in less than 1 Myr.

The maximum masses that planets can reach by pure pebble accretion are relatively low and thus the masses of the majority of the observed planets can probably not be explained via pebble accretion only. We also tested higher dust-to-gas ratios and a higher surface density (Fig. 10). Even though they do help in increasing the pebble isolation masses, they also bring longer or comparable timescales for planetary growth compared to the nominal simulations.

We also tested whether a higher planetary seed mass can shorten the growth timescales, by starting with $M_{init} = 0.1 M_{\oplus}$ instead of $M_{init} = 0.01 M_{\oplus}$. We find and show in Fig. 11 that even though the increased initial planetary mass shortens the growth timescale, the difference is very small and growing planets still fail to reach the isolation mass within the lifetime of the disc for $\alpha = 10^{-3}$. For discs with lower alpha values, even smaller initial embryos (0.01 Earth masses) can grow fast enough to reach pebble isolation mass before the end of the disc's lifetime.

The growth of planets via pebble accretion, can be aided by collisions either before or after the dissipation of the gas (Komi-

nami & Ida 2004; Cossou et al. 2014; Izidoro et al. 2017, 2019). It is also possible that the low pebble isolation masses we find mean that this formation mechanism leads to planet formation after gas disc dispersal rather than to planet formation during the gas disc phase. However, even with some collisions, the expected masses are not very high (Lambrechts et al. 2019), if the initial planetary masses are small. However, in order to reach a definite conclusion on this, future simulations including N-body interactions are needed.

We have shown in this work that a self-consistent treatment between the pebble sizes and disc structures is of crucial importance for planet formation simulations. In particular, we find that discs which support a large pebble isolation mass, also harbor low pebble accretion rates due to the small particle sizes, hence the growth timescales can be very long.

Acknowledgements. B.B. and S.S. thank the European Research Council (ERC Starting Grant 757448-PAMDORA) for their financial support. S.S. is a Fellow of the International Max Planck Research School for Astronomy and Cosmic Physics at the University of Heidelberg (IMPRS-HD).

References

- Ataie, S., Baruteau, C., Alibert, Y., & Benz, W. 2018, *A&A*, 615, A110
 Bai, X. N., Ye, J., Goodman, J., & Yuan, F. 2016, *ApJ*, 818, id. 152
 Batalha, N. M., Rowe, J. F., Bryson, S. T., et al. 2013, *ApJS*, 204, 24
 Bell, K. R. & Lin, D. N. C. 1994, *ApJ*, 427, 987
 Birnstiel, T., Dullemond, C. P., & Brauer, F. 2010, *A&A*, 513, A79
 Birnstiel, T., Klahr, H., & Ercolano, B. 2012, *A&A*, 539, A148
 Birnstiel, T., Ormel, C. W., & Dullemond, C. P. 2011, *A&A*, 525, A11
 Bitsch, B. 2019, *A&A*, 630, A51
 Bitsch, B. & Battistini, C. 2020, *A&A*, 633, A10
 Bitsch, B., Boley, A., & Kley, W. 2013, *A&A*, 550, A52
 Bitsch, B., Johansen, A., Lambrechts, M., & Morbidelli, A. 2015, *A&A*, 575, A28
 Bitsch, B., Lambrechts, M., & Johansen, A. 2015, *A&A*, 582, id.A112
 Bitsch, B., Morbidelli, A., Johansen, A., et al. 2018, *A&A*, 612, A30
 Bitsch, B., Raymond, S. N., & Izidoro, A. 2019, *A&A*, 624, A109
 Borucki, W. J., Koch, D., Basri, G., et al. 2010, *Science*, 327, 977
 Brauer, F., Dullemond, C. P., & Henning, T. 2008, *A&A*, 480, 859
 Brauer, F., Dullemond, C. P., Johansen, A., et al. 2007, *A&A*, 469, 1169
 Chen, J. & Kipping, D. 2017, *ApJ*, 834, 17
 Chiang, E. & Youdin, A. N. 2010, *Annual Review of Earth and Planetary Sciences*, 38, 493
 Chiang, E. I. & Goldreich, P. 1997, *ApJ*, 490, 368
 Cimerman, N. P., Kuiper, R., & Ormel, C. W. 2017, *MNRAS*, 471, 4662
 Cossou, C., Raymond, S. N., Hersant, F., & Pierens, A. 2014, *A&A*, 569, A56
 Drażkowska, J. & Alibert, Y. 2017, *A&A*, 608, A92
 Drażkowska, J., Li, S., Birnstiel, T., Stammer, S. M., & Li, H. 2019, *ApJ*, 885, 91
 Dubrulle, B., Morfill, G., & Sterzik, M. 1995, *Icarus*, 114, 237
 Dullemond, C. P. & Dominik, C. 2004, *A&A*, 417, 159
 Fortier, A., Alibert, Y., Carron, F., Benz, W., & Dittkrist, K. M. 2013, *A&A*, 549, A44
 Fressin, F., Torres, G., Charbonneau, D., et al. 2013, *ApJ*, 766, 81
 Fulton, B. J., Petigura, E. A., Howard, A. W., et al. 2017, *AJ*, 154, 109
 Gundlach, B. & Blum, J. 2015, *ApJ*, 798, 34
 Hartmann, L., Calvet, N., Gullbring, E., & D'Alessio, P. 1998, *ApJ*, 495, p.385
 Helled, R., Bodenheimer, P., Podolak, M., et al. 2014, in *Protostars and Planets VI*, ed. H. Beuther, R. S. Klessen, C. P. Dullemond, & T. Henning, 643
 Henning, T. & Mutschke, H. 1997, *A&A*, 327, 743
 Hudgins, D. M., Sandford, S. A., Allamandola, L. J., & Tielens, A. G. G. M. 1993, *ApJS*, 86, 713
 Ida, S. & Guillot, T. 2016, *A&A*, 596, L3
 Ida, S., Guillot, T., & Morbidelli, A. 2016, *A&A*, 591, A72
 Ikoma, M., Nakazawa, K., & Emori, H. 2000, *ApJ*, 537, 1013
 Izidoro, A., Bitsch, B., Raymond, S. N., et al. 2019, arXiv e-prints, arXiv:1902.08772
 Izidoro, A., Ogihara, M., Raymond, S. N., et al. 2017, *MNRAS*, 470, 1750
 Jäger, C., Dorschner, J., Mutschke, H., Posch, T., & Henning, T. 2003, *A&A*, 408, 193
 Johansen, A. & Bitsch, B. 2019, *A&A*, 631, A70
 Johansen, A. & Lacerda, P. 2010, *MNRAS*, 404, 475
 Johansen, A. & Lambrechts, M. 2017, *Annual Review of Earth and Planetary Sciences*, 45, 359

Johansen, A. & Youdin, A. 2007, *ApJ*, 662, 627
 Kamp, I. & Dullemond, C. P. 2004, *ApJ*, 615, 991
 Kobayashi, H., Tanaka, H., & Krivov, A. V. 2011, *ApJ*, 738, 35
 Kominami, J. & Ida, S. 2004, *Icarus*, 167, 231
 Lambrechts, M. & Johansen, A. 2012, *A&A*, 544, A32
 Lambrechts, M. & Johansen, A. 2014, *A&A*, 572, A107
 Lambrechts, M., Johansen, A., & Morbidelli, A. 2014, *A&A*, 572, A35
 Lambrechts, M. & Lega, E. 2017, *A&A*, 606, A146
 Lambrechts, M., Morbidelli, A., Jacobson, S. A., et al. 2019, *A&A*, 627, A83
 Lee, E. J., Chiang, E., & Ormel, C. W. 2014, *ApJ*, 797, 95
 Levison, H. F., Thommes, E., & Duncan, M. J. 2010, *AJ*, 139, 1297
 Mamajek, E. E. 2009, in *American Institute of Physics Conference Series*, Vol. 1158, *Exoplanets and Disks: Their Formation and Diversity*, ed. T. Usuda, M. Tamura, & M. Ishii, 3–10
 Martin, R. G. & Livio, M. 2015, *ApJ*, 810, 105
 Mathis, J. S., Rumpl, W., & Nordsieck, K. H. 1977, *ApJ*, 217, 425
 Millholland, S., Wang, S., & Laughlin, G. 2017, *ApJ*, 849, L33
 Morbidelli, A., Lambrechts, M., Jacobson, S., & Bitsch, B. 2015, *Icarus*, 258, 418
 Morbidelli, A. & Nesvorný, D. 2012, *A&A*, 546, A18
 Mulders, G. D., Pascucci, I., Apai, D., & Ciesla, F. J. 2018, *AJ*, 156, 24
 Muziolik, G. & Wurm, G. 2019, *ApJ*, 873, 58
 Ogiwara, M. & Ida, S. 2009, *ApJ*, 699, 824
 Ogiwara, M., Kokubo, E., Suzuki, T. K., & Morbidelli, A. 2018, *A&A*, 615, A63
 Ormel, C. W. & Klahr, H. H. 2010, *A&A*, 520, A43
 Ormel, C. W., Liu, B., & Schoonenberg, D. 2017, *A&A*, 604, A1
 Paardekoooper, S. J. & Mellema, G. 2006, *A&A*, 459, L17
 Petigura, E. A., Howard, A. W., & Marcy, G. W. 2013, *Proceedings of the National Academy of Science*, 110, 19273
 Pollack, J. B., Hubickyj, O., Bodenheimer, P., et al. 1996, *Icarus*, 124, 62
 Poppe, T., Blum, J., & Henning, T. 2000, *ApJ*, 533, 454
 Preibisch, T., Ossenkopf, V., Yorke, H. W., & Henning, T. 1993, *A&A*, 279, 577
 Rafikov, R. R. 2004, *AJ*, 128, 1348
 Raymond, S. N., Boulet, T., Izidoro, A., Esteves, L., & Bitsch, B. 2018, *MNRAS*, 479, L81
 Ros, K. & Johansen, A. 2013, *A&A*, 552, A137
 Ros, K., Johansen, A., Riipinen, I., & Schlesinger, D. 2019, *A&A*, 629, A65
 Savvidou, S., Bitsch, B., & Lambrechts, M. 2020, *A&A*, 640, A63
 Schoonenberg, D., Liu, B., Ormel, C. W., & Dorn, C. 2019, *A&A*, 627, A149
 Schoonenberg, D. & Ormel, C. W. 2017, *A&A*, 602, A21
 Shakura, N. I. & Sunyaev, R. A. 1973, *A&A*, 500, 33
 Surville, C., Mayer, L., & Alibert, Y. 2020, *arXiv e-prints*, arXiv:2009.04775
 Suzuki, T. K., Ogiwara, M., Morbidelli, A., Crida, A., & Guillot, T. 2016, *A&A*, 596, id.A74
 Testi, L., Birnstiel, T., Ricci, L., et al. 2014, in *Protostars and Planets VI*, ed. H. Beuther, R. S. Klessen, C. P. Dullemond, & T. Henning, 339
 Venturini, J., Guilera, O. M., Haldemann, J., Ronco, M. P., & Mordasini, C. 2020a, *arXiv e-prints*, arXiv:2008.05513
 Venturini, J., Guilera, O. M., Ronco, M. P., & Mordasini, C. 2020b, *arXiv e-prints*, arXiv:2008.05497
 Warren, S. G. & Brandt, R. E. 2008, *Journal of Geophysical Research (Atmospheres)*, 113, D14220
 Weidenschilling, S. J. 1977, *MNRAS*, 180, 57
 Weidenschilling, S. J. 1980, *Icarus*, 44, 172
 Weidenschilling, S. J. 1984, *Icarus*, 60, 553
 Weiss, L. M., Isaacson, H. T., Marcy, G. W., et al. 2018, *AJ*, 156, 254
 Wu, Y. 2019, *ApJ*, 874, 91
 Youdin, A. & Johansen, A. 2007, *ApJ*, 662, 613
 Youdin, A. N. & Goodman, J. 2005, *ApJ*, 620, 459
 Zeng, L., Jacobsen, S. B., Sasselov, D. D., et al. 2019, *Proceedings of the National Academy of Science*, 116, 9723
 Zhu, W., Petrovich, C., Wu, Y., Dong, S., & Xie, J. 2018, *ApJ*, 860, 101
 Zsom, A., Ormel, C. W., Dullemond, C. P., & Henning, T. 2011, *A&A*, 534, A73
 Zsom, A., Ormel, C. W., Güttler, C., Blum, J., & Dullemond, C. P. 2010, *A&A*, 513, A57

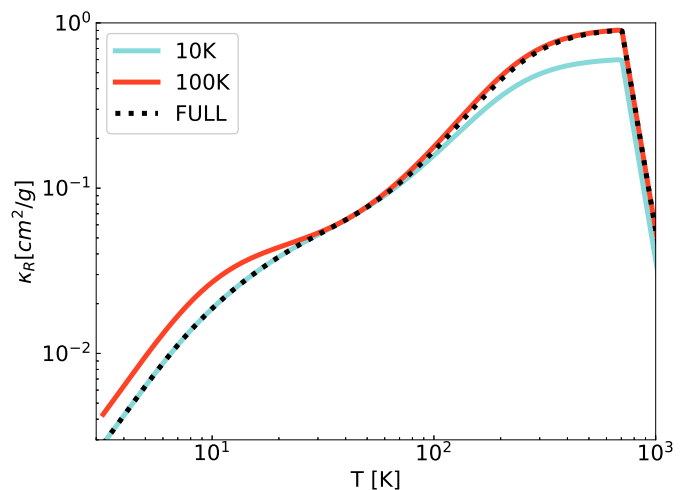


Fig. A.1: Rosseland opacity as a function of temperature for FeS calculated using refractive indices measured at two different temperatures. The black dashed line shows the opacity we use here which combines the opacities derived from the two temperatures.

Appendix A: Refractive indices

In Table 1 we include the sources of the refractive indices used in order to calculate the opacities per grain size and composition as a function of temperature. The refractive indices are not only dependent on the wavelength of the incident radiation, but on the temperature of the surrounding medium, too. Hence, we find for some of the species used in this work different refractive indices for measurements at different temperatures.

From Henning & Mutschke (1997), we obtain refractive indices as a function of wavelength for FeS measured at $T = 10$ and 100 K. In our disc models we assume that the dust temperature is the same as the temperature of the surrounding gas, which is a good approximation for the optically thick parts of the disc (Kamp & Dullemond 2004). For this reason, we choose to combine the refractive indices obtained for different temperatures, so that the new refractive indices correspond to the values for $T = 10$ K for low temperatures but gradually switch to the values corresponding to $T = 100$ K for high temperatures. In Fig. A.1 we show the Rosseland opacity as a function of temperature, calculated with the refractive indices measured at $T = 10$ and 100 K and the combination of those which we use in the opacity module of this work.

In Hudgins et al. (1993), the refractive indices are given for CO_2 for $T = 10, 30, 50$ and 70 K. We plot the resulting Rosseland opacities for some of those different measurements in Fig. A.2a. We choose to only use the refractive indices for 50 K in our simulations because the differences are very small between the three different sets.

Similarly, for CH_4 we find refractive indices for $T = 10, 20$ and 30 K. The resulting mean Rosseland opacities are plotted in Fig. A.2b. They are almost the same, independently of the temperature at which the measurement was made. We chose for this work to use the refractive indices at $T = 20$ K.

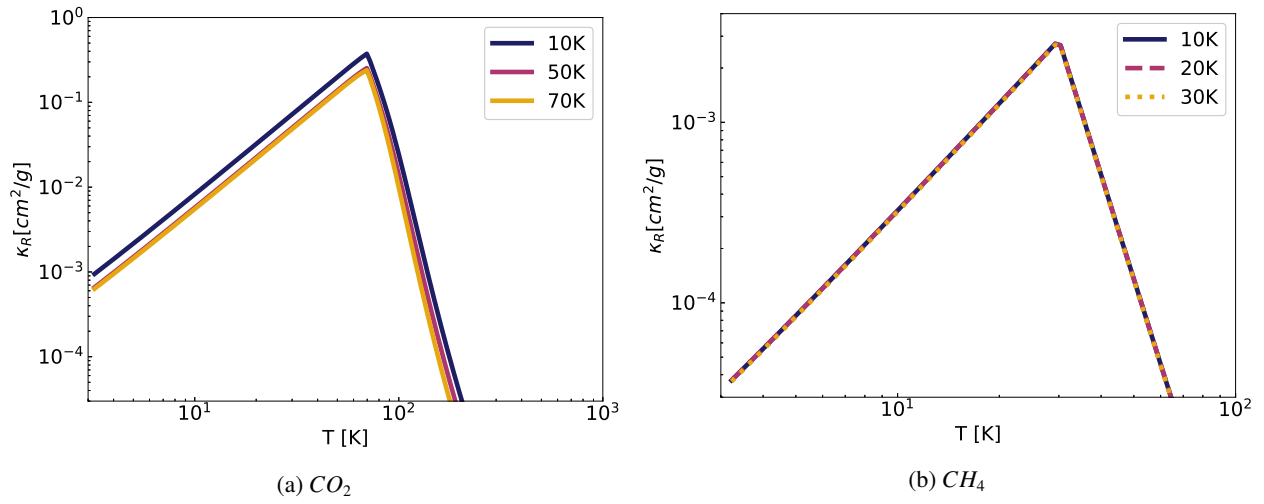


Fig. A.2: Rosseland opacity as a function of temperature for the specified species calculated using refractive indices measured at three different temperatures.